Raman spectroscopy for real-time concurrent detection of multiple scalants on RO membranes

Danielle J. Park [a,*], Omkar D. Supekar [a,b], Victor M. Bright [a], Alan R. Greenberg [a,c], Juliet T. Gopinath [b,d,e]

[a] Department of Mechanical Engineering, University of Colorado, Boulder, CO 80309, USA
[b] Department of Electrical, Computer, and Energy Engineering, University of Colorado, Boulder, CO 80309, USA
[c] Membrane Science, Engineering and Technology Center, University of Colorado, Boulder, CO 80309, USA
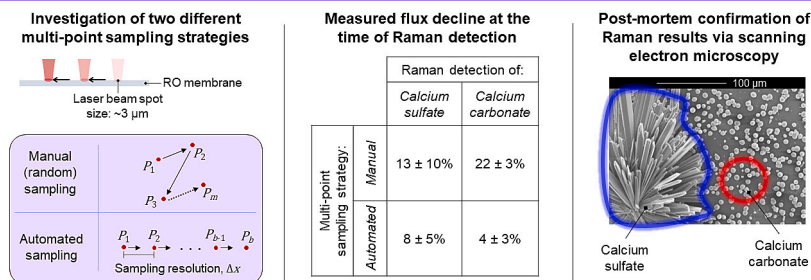[d] Department of Physics, University of Colorado, Boulder, CO 80309, USA
[e] Materials Science and Engineering Program, University of Colorado, Boulder, CO 80309, USA

HIGHLIGHTS

- Real-time, concurrent detection of gypsum and calcite scaling using Raman spectroscopy
- Raman results confirmed by post-mortem SEM analysis and gravimetric measurements
- Improved detection results obtained using an automated sampling methodology
- Early Raman detection of mixed-salt scaling achieved at low values of flux decline

GRAPHICAL ABSTRACT

ARTICLE INFO

ABSTRACT

In-situ monitoring techniques of reverse osmosis (RO) desalination systems, particularly those with chemical sensing capabilities, can provide the means for better understanding important scaling mechanisms as well as early scaling detection. In this work, both calcium sulfate and calcium carbonate scaling on RO membranes were detected concurrently in real time using Raman spectroscopy to provide a unique chemical fingerprint. Two different sampling methodologies (manual and automated) were employed, and their performance was evaluated by comparing the Raman detection times to concurrent values of flux decline. The manual sampling strategy resulted in the detection of calcium sulfate and calcium carbonate at mean permeate flux declines of 13 ± 10 % and 22 ± 3 %, respectively. The automated sampling strategy provided better performance, with detection of calcium sulfate and calcium carbonate at mean flux declines of 8 ± 5 % and 4 ± 3 %, respectively. The increased sensitivity and decreased variability of the automated sampling strategy provided valuable preliminary insights for the selection of optimized sampling strategies. The ability to identify the chemical composition of different scaling crystals including their polymorphs is an important step toward better understanding of the crystallization pathways of multi-component feed streams used in seawater and brackish water RO desalination.

* Corresponding author.
E-mail address: danielle.j.park@colorado.edu (D.J. Park).

1. Introduction

In membrane-based desalination, supersaturated levels of dissolved ions of sparingly soluble salts in the feed water can cause the formation of crystalline salt. These crystals can either form in the bulk solution and subsequently deposit on the membrane surface, or form directly on the membrane surface—both pathways effectively reducing the active membrane area [1–5]. This undesirable effect is known as membrane scaling. Generally, the negative consequences of scaling include increased energy consumption, higher operating costs, decreased membrane performance, and shorter membrane lifespans [3,6,7].

Traditional RO desalination performance metrics such as permeate flux, pressure drop, and salt rejection have been used to detect scaling onset as well as to better understand scaling mechanisms [4,8–10], both goals geared toward mitigating membrane scaling. However, these metrics reflect the overall (global) conditions of the membrane, providing area-averaged measurements. Thus, their use can pose certain difficulties in detecting spatially dependent changes occurring on the membrane such as scaling. Furthermore, these metrics do not identify the chemistry of the scalant(s). As a workaround, global metrics have been utilized in conjunction with membrane autopsies and scanning electron microscopy/energy-dispersive X-ray spectroscopy (SEM/EDS) to determine the source and severity of scaling [11–13]. However, EDS provides only elemental analysis, and the destructive nature of the autopsy makes it difficult to implement in real time the insights gained from the analysis.

As a result, in-situ real-time monitoring techniques have been identified as a critical area of need in RO desalination [4,14–32]. Among these techniques, those that have focused on inorganic scaling typically utilize synthetic feedwaters containing precursors for single-salt scaling (e.g., CaSO₄ only or CaCO₃ only). However, single-salt scaling can result in significantly different behavior and morphology as compared to mixed-salt scaling (i.e., scaling in the presence of many competing scale-forming ions) [33–35]. While the RO desalination literature contains relatively few mixed-salt scaling studies [34,36], such information is critical since natural feedwaters contain multiple scaling ions that typically generate a mixture of scalants. In addition, although in-situ monitoring techniques may provide higher sensitivity to early onset scaling as compared to global metrics, more localized measurements also run the risk of providing false negative detection results due to unrepresentative sampling. Therefore, the placement, configuration, and sampling strategy of local sensors are important factors that must be considered.

Raman spectroscopy is an analytical technique based on a light-matter interaction, known as Raman scattering, which can provide a real-time chemical 'fingerprint' of a material. Here, incident photons from a laser source interact with the material's optical phonons (high-frequency vibrations [37]), generating inelastically scattered photons [38]. The energy difference (i.e., change in wavelength) between the incident and scattered photons is specific to the rotational and vibrational transitions of particular bonds in a molecule, enabling chemical 'fingerprinting.' Accordingly, Raman spectroscopy is an attractive real-time chemical sensing technique that could provide improved understanding of mixed-salt scaling dynamics during RO desalination. Furthermore, the success of many of the strategies used in scale control would benefit from accurate chemical identification of the scales during their formation [39,40]. Given that chemical sensing is not an integrated capability of well-studied real-time monitoring techniques, the distinctive ability of Raman spectroscopy to provide chemical identification offers the opportunity to better understand multi-component scaling behavior during RO desalination.

In the literature, Raman spectroscopy has been utilized as a real-time sensor to detect vanillin on ultrafiltration (UF) membranes [29,41], bacteria on microfiltration (MF) membranes [30], and single-component scalants on RO membranes [31,32,42]. Both calcium sulfate and calcium carbonate were concurrently detected using ex-situ Raman spectroscopy in previous work [32]. In the present work, we report successful real-time detection of membrane scaling from a two-salt feed solution, using a Raman microscope with a static (fixed) objective that is integrated with a specially designed bench-scale RO crossflow cell mounted on a movable stage. Replicate scaling experiments were conducted, during which real-time Raman spectra (obtained from the membrane surface) and permeate flux were simultaneously recorded. The permeate flux data serve as a key benchmark to which Raman data can be compared, as the decrease in permeate flux over time is commonly used as a metric of membrane performance. The scaling experiments utilize synthetic salt solutions containing precursors for calcium sulfate and calcium carbonate scale formation, as these are commonly encountered scales in RO desalination. These mixed-salt scaling studies better reflect scaling conditions associated with natural feedwaters. Consequently, this work serves as an important step in mixed-salt scaling studies focused on early detection and better understanding of scaling mechanisms, leading to critical insights for improved scale control in industrial RO desalination systems.

2. Materials and methods

2.1. RO system and experimental design

Design considerations for a suitable RO system included filtration configuration, data storage, maximum operating time, and requirements for handling/waste disposal. Calcium sulfate and calcium carbonate were selected as model scalants as they are commonly encountered in brackish water RO desalination [4,43]. Accordingly, an extra-low energy reverse osmosis membrane (Toray 73HA) designed for brackish feed waters was selected for use in all scaling experiments.

The objective of the experimental design was to investigate real-time detection of more than one scalant from a multi-component feed stream using Raman spectroscopy. Representative Raman sampling was an important design driver given that the in-house Raman microscope constituted a single, fixed-point laser beam spanning ~3 μm in diameter (at full width, half maximum), i.e., a point measurement, compared to the much larger active membrane area of 218.8 cm² (12.5 cm × 17.5 cm). Based on the research objective and the need for representative sampling, two sampling strategies were devised and evaluated, each in a series of replicate, proof-of-concept experiments. The real-time Raman response to membrane scaling by calcium sulfate and calcium carbonate was compared to permeate flux decline, a global metric of membrane performance.

2.2. Instrumentation design

An existing reverse osmosis (RO) and Raman microscope system utilized in a single-salt scaling study [44] was modified for use in the present work. The major components of the system are shown in Fig. 1.

The RO system was operated in total recycle mode in which the permeate and retentate streams were continuously directed back to the feed tank. An in-line flow sensor was used to measure the permeate volumetric flow rate before its return to the feed tank. A 0.2 μm PES filter was installed downstream of the flow cell to remove any particulates in the retentate stream. In addition, prior system cleaning minimized the deposition of loose scaling crystals formed in the bulk feed or released from any buildup in the RO system. These measures have been reported to successfully minimize bulk crystallization in benchtop scaling experiments [2,3].

The construction details of the custom-built plate-and-frame RO flow cell were described in a previous work [44]. In brief, the flow cell featured a rectangular optical window that interfaced with the objective (11 mm working distance) of the Raman microscope. The flow cell was mounted on x- and y-axis translational stages allowing the fixed-coordinate Raman laser beam to sample different locations on the membrane through the rectangular optical window of the flow cell. For

fine adjustment of the laser beam focus, a *z*-axis translational stage with submicron resolution (Thorlabs, MLJ150) was used to adjust the height of the flow cell. Two manual *x*- and *y*-axis translational stages (Thorlabs, LT1) mounted on top of the *z*-axis stage were used in a first series of experiments (Series I). In a second series of experiments (Series II), the manual *x*-axis stage was upgraded to a motorized stage (Zaber, X-LSM150A).

2.2.1. Manual sampling

In Series I experiments, we collected real-time Raman spectra (*RS*) from multiple points on the membrane surface by manually adjusting the Raman sampling location (i.e., manual, multi-point sampling) during scaling experiments. Under a fixed-coordinate Raman laser beam (Fig. 2), manual *x*-axis and *y*-axis translational stages adjusted the positioning of the flow cell. For each sequentially sampled point, both stages were simultaneously and manually adjusted such that the laser beam focused on a random location on the membrane, within a pre-defined 4 mm^2 region of interest (ROI). The ROI was positioned downstream of the membrane due to its higher scaling propensity, caused by increasing concentration polarization with increasing axial position, *x*. At each sampled (x_m, y_m) location, a set of Raman spectra ({*RS*}) was collected for $n = 10$ min approximately every minute, before moving onto the next position for a total of *m* positions.

2.2.2. Automated sampling

In the Series II experiments, Raman spectra (*RS*) were recorded using an *automated* multi-point sampling strategy. Prior to the beginning of the scaling experiment, the *y*-axis manual stage was used to adjust the flow cell position such that the optical window was centered under the microscope objective, along the *y*-axis. The *x*-axis motorized stage was initialized to a downstream region of interest (ROI). Then, during real-time Raman spectral acquisition, the motorized stage was programmed to move in linear increments (i.e., with a spatial sampling resolution, Δx) for a total sampled length, ΔL (Fig. 3). Consequently, the total number of sequentially sampled points was $b = \left(\frac{\Delta L}{\Delta x}\right) + 1$.

The selection of *b* total sampled points was informed by the distances between the largest scaling species and the smallest scaling species. Based on SEM images of Series I membrane samples, gypsum was the larger scaling species with crystal distances that were on the order of millimeters while calcium carbonate was the smaller scaling species with crystal spacings on the order of 10's of microns. Consequently, a total sampled length (ΔL) of 4.5 mm was selected. Since an important goal in early-stage scaling detection is to minimize the temporal sampling resolution, Δt, the minimum Raman acquisition time per sampled point was first determined. A 10 s acquisition time was selected with two accumulations (averaged spectra) to improve signal-to-noise ratios (SNR), and an additional ~20 s was added to the sampling time to provide ample time for data acquisition and storage, resulting in the acquisition of one Raman spectrum every ~30 s. Based on a goal of $\Delta t < 5$ min for the sampling cycle time, where $\Delta t = b \times 30$ s, a spatial resolution of $\Delta x = 0.5$ mm was selected.

2.2.3. Real-time Raman data

Proprietary software (LightField, Princeton Instruments) was used in the real-time acquisition of Raman data, and a Raman spectral range of 100–1300 cm^{-1} was selected to capture the Raman bands of calcium sulfate and calcium carbonate. There are several different polymorphs that can form in the crystals systems of calcium sulfate (CaSO$_4$) and calcium carbonate (CaCO$_3$). The most stable form of calcium sulfate is
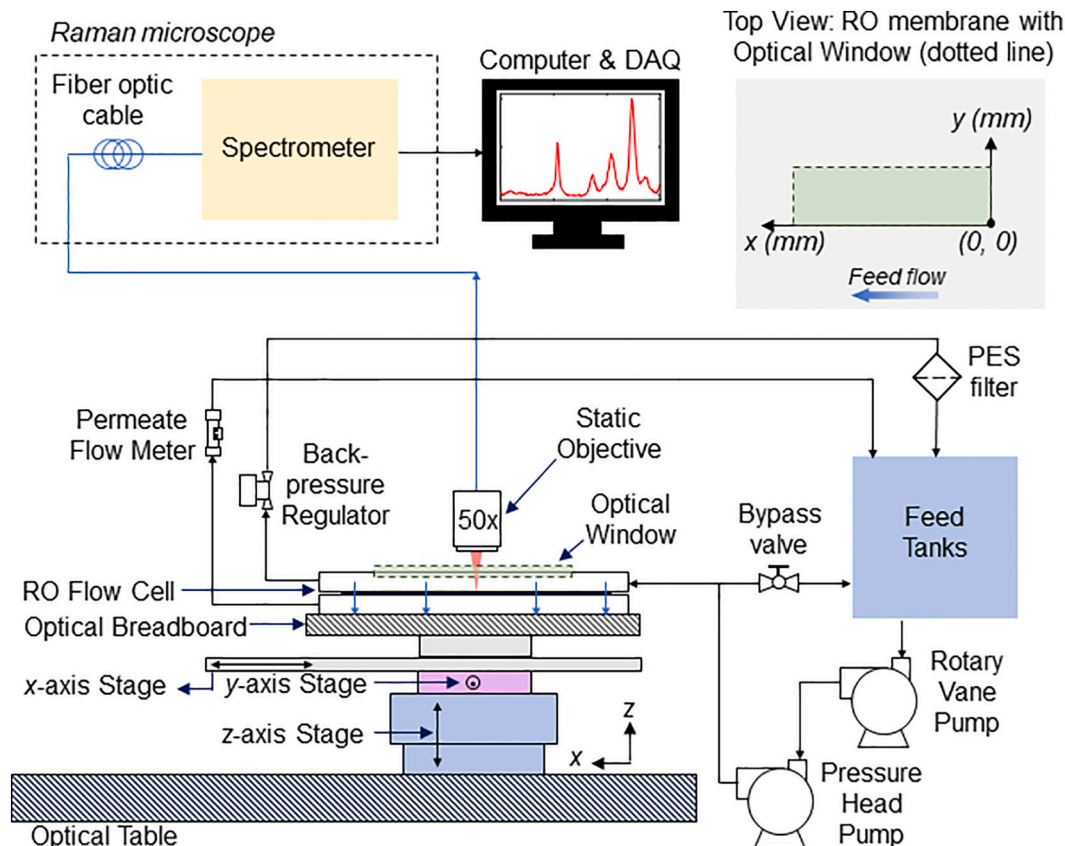

Fig. 1. Schematic of the RO system and integrated components for real-time measurement of permeate flux and Raman spectra. The *x*- and *y*-axis translational stages adjusted the flow cell position under the fixed microscope objective. The z-axis translational stage adjusted the height of the flow cell to focus the laser beam on the membrane surface. Manual sampling occurred in a 2 mm × 2 mm window, centered at approximately $(x, y) = (84$ mm, 16 mm$)$. Automated sampling began at approximately $(x, y) = (76$ mm, 16 mm$)$.
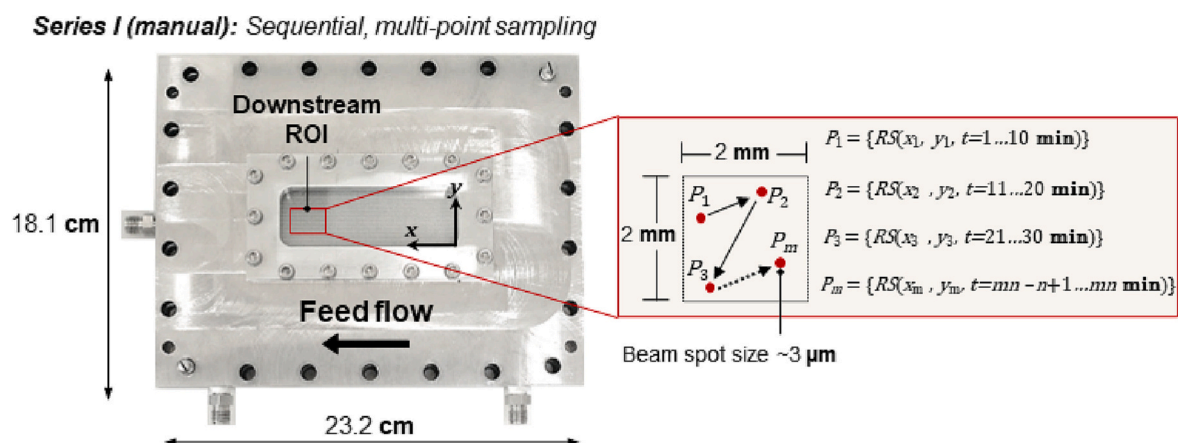
Fig. 2. The reverse osmosis flow cell (left) and schematic of manual, multi-point detection (right). Manual x- and y-axis translational stages were adjusted to reposition the flow cell in the downstream region of interest (ROI) during real-time Raman detection. For time $t = 1\ldots10$ min, acquisition of a Raman spectral set $\{RS\}$ began at position $P_1 = (x_1, y_1)$, every minute. P_2 represented the Raman spectra collected at a second randomly selected location, and similarly through position P_m. The collection time, n, is 10 min at each point. In this manner, Raman spectra were collected at randomly selected positions until both scaling salts were detected in at least one location.
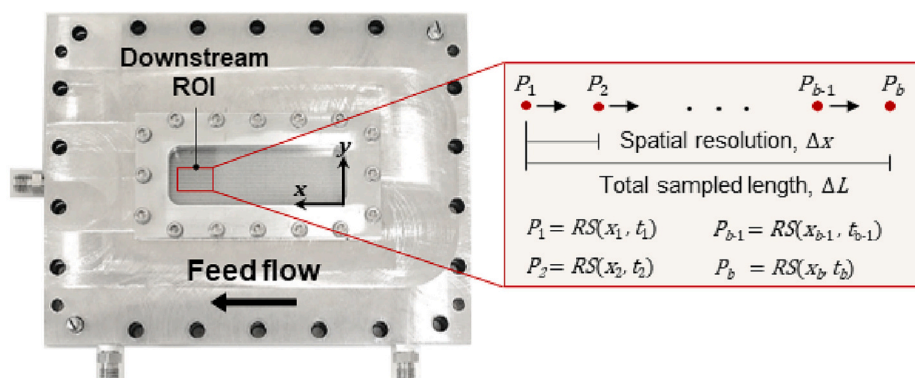
Fig. 3. The reverse osmosis flow cell (left) and schematic of automated, multi-point sampling (right). A motorized x-axis stage allowed for sequential, linear Raman sampling along a predefined sampled length (ΔL) with increments of the predefined spatial resolution (Δx). A Raman spectrum was acquired at position P_1, at location x_1 and time t_1. Location x_b and time t_b represented the Raman spectrum obtained at the last sampled point, completing one full cycle of 'b' sampled points. A new sampling cycle resumed at location x_1 until both scaling salts were detected in at least one location or at the end of 2 h, whichever came first.

gypsum (CaSO$_4 \bullet$2H$_2$O), which has a strong ν_1 vibrational mode at a Raman shift of 1008 cm^{-1} [45]. Calcium carbonate, which can exist in three main polymorphs (calcite, vaterite, and aragonite), has ν_1 vibrational modes occuring at Raman bands 1080–1090 cm^{-1} due to the symmetric stretching mode of the carbonate ion [46].

The Raman microscope was operated with an incident power of ~27 mW on the sample. Raman data preprocessing included baseline removal to subtract the fluorescent background signal, cosmic ray removal, and vector normalization to account for fluctuations in the incident power on the sample [44]. Subsequently, spectral intensity values were taken as ratios to the membrane's C-O-C stretching band at 1150 cm^{-1} (most prominent membrane Raman band [47]). The ratio values are hereafter referred to as the relative Raman intensity. Raman detection of a scalant was defined to occur when the relative Raman intensity of the scalant Raman band exceeded a threshold value of two standard deviations above its mean relative intensity value during compaction in DI water [44]. This was to ensure that any noisy scalant Raman signals were not taken as false positive detection events.

2.3. Experimental procedure

Prior to initiating the scaling experiments, the RO system was cleaned using 2–3 cycles of deionized water flushes until in-line conductivity readings sustained values <1 μS/cm for at least 30 min. In some cases, this was followed by an additional system flush of <1 %

hydrogen peroxide and two cycles of deionized water flushes. Stock rolls of commercial reverse osmosis membranes (Toray UTC-73HA) were stored in a plastic bag with DI water to prevent dry out. To prepare a membrane for a scaling experiment, it was first cut to size from a stock roll and soaked in a 50 % solution of isopropanol for at least 30 min and rinsed with DI water to remove any residual alcohol. The membrane was then installed in the RO flow cell for filtration of a DI water feed at 1 MPa for 12 to 15 h overnight to minimize any permeate flux decline due to membrane compaction. Operating conditions were recorded using a data acquisition system. During both compaction and scaling phases of the experiments, in-line sensors were used to record the feed pressure, volumetric flow rate, and temperature at approximately one-minute intervals.

To initiate the scaling portion of a scaling experiment, the prepared salt solution was pumped into the flow cell at a volumetric flow rate of 25 L/h (crossflow velocity of ~3.0 cm/s) from a temperature-controlled carboy kept at 23.5 ± 0.5 °C. The desired initial permeate flux (related to the transmembrane pressure) and volumetric flow rate were set once at the start of the experiment by iteratively adjusting a backpressure regulator and bypass valve. The transmembrane pressure varied from 1.05 to 1.25 MPa (~150 to 180 psi) to maintain an initial permeate flux that was constant between replicate scaling experiments. After extensive preliminary investigation, a feed composition and RO operating pressure (i.e., initial permeate flux) were selected for Series I (Tests 1–3, Table 1) to produce a dense formation of scaling crystals on the

membrane surface over a reasonable timescale (< 8 h). This would effectively increase the chances of successful Raman detection of both salts in real-time, given the single, fixed-coordinate laser beam of the Raman microscope configuration.

Synthetic salt solutions were prepared to include precursors of both calcium sulfate and calcium carbonate scaling, shown in Table 1. Calcium sulfate dihydrate (CaSO$_4$·2H$_2$O, ReagentPlus, ≥99 %, Sigma Aldrich) was first added to deionized water and stirred vigorously for 12–18 h. Next, calcium chloride (CaCl$_2$, anhydrous powder, ≥97 %, Sigma Aldrich) was added to the CaSO$_4$ salt solution since calcium chloride has a significantly higher solubility than that of calcium sulfate dihydrate. To avoid premature precipitation of CaCO$_3$ during synthesis of the salt solution, sodium bicarbonate (NaHCO$_3$, 99 + %, extra pure, Acros Organics) was added to the feed solution just at the start of the scaling experiment [32].

Although all membrane samples came from the same batch of stock membranes, Series II (Tests 4–9, Table 1) membranes exhibited a lower initial permeate flux than that of Series I membranes, likely due to some dehydration of the membranes during storage [32]. Here, low permeate fluxes would undesirably cause a decrease in the extent of scale coverage and consequently reduce the chances of representative Raman detection, once again, due to the fixed-coordinate sensor configuration. The solute concentration at the membrane wall (C_{wall}), which is exponentially proportional to the permeate flux (J_v), directly influences the severity of membrane scaling as seen in Eq. (1) [2], with R as salt rejection and k_m as the mass-transfer coefficient.

$$CP = \frac{C_{wall}}{C_{bulk}} = (1 - R) + R \bullet exp\left(\frac{J_v}{k_m}\right) \quad (1)$$

To compensate for the lower, initial permeate fluxes of the membranes tested in Series II, the bulk feed concentration was increased to increase the average CP modulus at the membrane wall. In the estimation of the average CP modulus, J_v was the measured average initial permeate flux, R was assumed to be 1 (complete solute rejection), and k_m was calculated using the method described in a previous work [44,48], whose axial length-averaged value was calculated to be ~1.3 × 10^{-3} cm/s. This resulted in scaling conditions at the membrane wall for Series II that were closer to that of Series I, thereby ensuring a more dense coverage of the membrane surface by scaling crystals.

For simplicity, only major scaling ions (Ca^{2+}, CO$_3^{2-}$, and SO$_4^{2-}$) were considered in the estimation of saturation indices, SI (Eq. (2)), with respect to calcite and gypsum, using PHREEQC Interactive 3.7.0 software [49].

$$SI = log\left(\frac{IAP}{K_{sp}}\right) \quad (2)$$

2.4. Post-mortem metrics

After the completion of each scaling experiment, the RO membrane was promptly removed from the flow cell and dried in ambient air. Scaled membranes from Tests 1–9 were cut into downstream and upstream coupons measuring 1 cm × 3 cm. It was ensured that the downstream coupons incorporated the region of downstream real-time Raman detection (Fig. 4). Post-mortem characterization of the prepared membrane coupons was conducted to complement the real-time data and provide more insight into the performance of the Raman sensor during scaling detection.

The mass of the scaled membrane coupons (Tests 1–9) was measured using a microbalance (ME 235S, Sartorious). The mass measurements were normalized to the dimensions of the coupons, measured using a digital caliper (DCLA 0605, VINCA). Gravimetric measurements of the scaled membranes were compared to that of virgin membrane coupons. The virgin membranes underwent the same pretreatment as the scaled membranes, which included a 30-min soak in a solution of 50 % isopropanol and 12–15 h period of compaction at 1 MPa in DI water. After completing the gravimetric measurements, the prepared membrane coupons were sputter-coated with ~4–6 nm of platinum to prevent sample charging during scanning electron microscopy (SEM, Hitachi SU3500). The treated membrane coupons underwent SEM analysis to confirm the presence of both calcium sulfate and polymorphs of calcium carbonate crystals on the membrane.

3. Results and discussion

3.1. Manual sampling (series I)

In Series I experiments, three replicate scaling tests (Tests 1–3) were conducted using manual (random) sampling within the predefined downstream region of interest (2 mm × 2 mm). Representative real-time Raman data from a Series I test are shown in Fig. 5a.
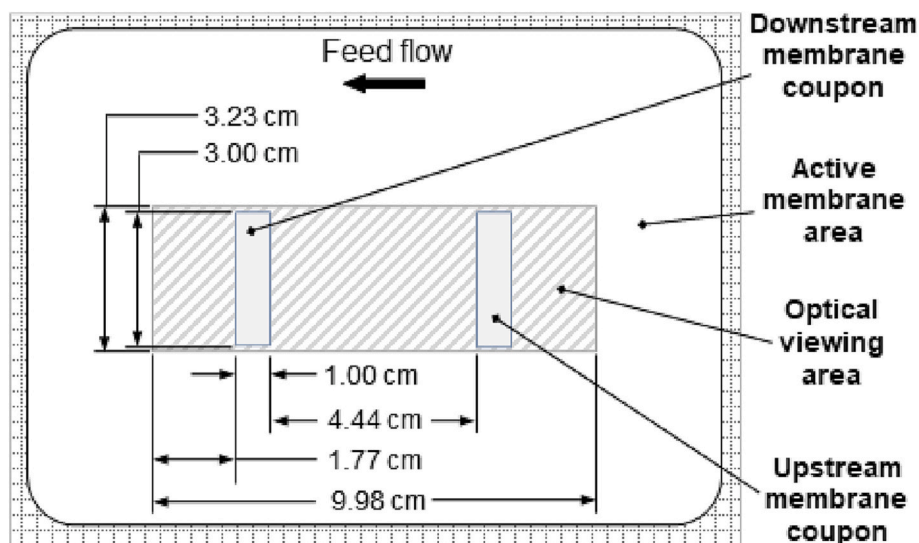
Here, gypsum (blue triangle) was detected at the manually-sampled Positions 4 and 5 starting at $t = 45$ min, where the CaSO$_4$ relative Raman intensity surpassed the detection threshold line (solid blue line). In Fig. 5b, a representative Raman spectrum from Position 4 shows a clear peak at 1008 cm^{-1}, which belongs to gypsum (CaSO$_4$•2H$_2$O). Calcium carbonate (red circle) was detected at Position 14 at $t = 172$ min, where the CaCO$_3$ Raman intensity exceeded the dotted red detection threshold line. A corresponding Raman spectrum from Position 14 (Fig. 5c) shows a broad peak extending from 1086 to 1090 cm^{-1}, which is indicative of both the calcite and vaterite polymorphs of calcium carbonate.

Results for gypsum and calcium carbonate Raman detection are summarized in Tables 2 and 3. These tables indicate the time elapsed until the Raman signal of a scaling salt exceeded its detection threshold value (Raman detection time), the permeate flux decline at the time of Raman detection, and the percentage of total sampled points that resulted in a positive Raman detection result.

In the Series I tests, the mean percentage of sampled points with positive gypsum Raman detection was 27 ± 14 %. The percentage of sampled points with positive calcium carbonate Raman detection was lower than that of gypsum with a mean of 9 ± 2 %. Given the small and randomly-selected Raman sampling areas, this comparison suggests that the calcium carbonate crystals occupied a smaller total surface area, which would lead to a lower probability of detecting a calcium carbonate crystal. This is further supported by the greater relative Raman intensity of gypsum compared to that of calcium carbonate in Fig. 5b

Table 1
Test conditions for Series I and II experiments.

Test #	Membrane Performance	Bulk Feed: Composition			Bulk Feed: Saturation Index (*SI*)		Membrane Wall: Average CP Modulus	Membrane Wall: Saturation Index (*SI*)	
	Average initial permeate fiux	CaSO$_4$•2H$_2$O	CaCl$_2$	NaHCO$_3$	Gypsum	Calcite		Gypsum	Calcite
	(L/m²/h)	(mM)	(mM)	(mM)					
1–3	49	8.4	1.7	2.0	−0.45	0.21	3.2	0.20	0.99
4–9	37	10.5	3.4	4.0	−0.30	−0.02	2.4	0.19	0.57

Fig. 4. After each scaling experiment was terminated, the membrane was removed from the flow cell in under ~5 min and dried in ambient air. Membrane coupons were cut to size from the downstream and upstream regions, such that the downstream coupon incorporated the region of real-time Raman detection. Gravimetric analysis was first performed on these coupons, due to the sample coating required for scanning electron microscopy.

and c, respectively, where the gypsum Raman band at 1008 cm^{-1} is observed to rival the C-O-C stretching band of the membrane at 1150 cm^{-1}. The relative Raman intensity of calcium carbonate, however, remains low compared to the 1150 cm^{-1} band.

Gypsum was detected after 100 ± 53 min of scaling and calcium carbonate was detected at 161 ± 18 min. Flux decline at the time of calcium sulfate and calcium carbonate Raman detection was 13 ± 10 % and 22 ± 3 %, respectively. In general, sufficiently sensitive detection with respect to permeate flux decline was not demonstrated, considering that a flux decline of 10–15 % typically warrants remediation measures [50]. There was one instance of early detection, during Test 1, where gypsum detection occurred at a flux decline of only 1 %; however, consistency in early detection is an important objective of the technique. It follows that a more systematic sampling approach is needed for more consistent detection. Therefore, an automated sampling approach was implemented using the Series II sampling strategy.

3.2. Automated sampling (Series II)

In Series II experiments, six replicate scaling tests (Tests 4–9) were conducted using the automated sampling strategy. Representative real-time data from a Series II test are shown in Fig. 6a.

Here, calcium sulfate was first detected at $x = 79.5$ mm and $t = 59$ min, where the gypsum ($CaSO_4 \bullet 2H_2O$) relative Raman intensity surpassed the solid blue threshold value. In Fig. 6b, a representative Raman spectrum sampled from the $x = 79.5$ mm position shows the characteristic peak of gypsum at 1008 cm^{-1}. Calcium carbonate was detected at the $x = 76.0$ mm position at $t = 79$ min (Fig. 6c), where the calcium carbonate Raman intensity is observed to exceed the dotted red threshold value. The Raman spectrum at this time reveals a broad peak encompassing wavenumbers from 1080 to 1086 cm^{-1}. This suggests the presence of some amorphous calcium carbonate (ACC) because the amorphous form of calcium carbonate contains highly disordered C—O bonds resulting in a broad band at ~1080 cm^{-1} [51]. The polymorphic differences observed between the Series I and II calcium carbonate crystals may be attributed to the different feed compositions utilized (Table 1) and demonstrates the potential of the present Raman methodology to differentiate varying crystalline structures of the scaling salts.

Series II results for gypsum and calcium carbonate Raman detection are summarized in Tables 4 and 5. It is interesting to note that the mean

percentage of sampled points with positive calcium carbonate detection (27 ± 8 %) was significantly higher than that of the previous Series I tests (9 ± 2 %). However, the mean percentage of sampled points with positive gypsum detection did not demonstrate as large a change (27 ± 14 % and 20 ± 15 % for Series I and II, respectively). This suggests that the more systematic sampling strategy employed in the Series II experiments improved upon the random Series I sampling strategy for detection of calcium carbonate scale. We propose that the automated sampling employed in Series II experiments provided an effective increase in sampling area, which would improve the chances of detecting smaller crystals such as calcium carbonate [52–54]. In random sampling, on the other hand, the selection of the next sampled point does not take into consideration the location of the previously sampled point (i.e., is less systematic), so it favors the detection of larger crystals such as gypsum [23,55].

In Test 6, no gypsum was detected within the predefined downstream detection period of 2 h, although SEM imaging confirmed the presence of gypsum crystals. This result exemplifies a false negative outcome that can be attributed to the limited sampling area. In contrast, visual observation techniques such as EXSOD/MeMo [16,17,43] have a larger optical sampling area compared to the current Raman sampling scheme (on the order of cm^2 instead of mm^2). This eliminates the need for waiting periods to sample multiple points and reduces the chances of obtaining a false negative detection result. However, successful scale detection by visual observation requires that the crystal or group of crystals grow to ~50 μm in diameter, whereas the Raman sensor can detect crystals of smaller dimensions [44,53]. Furthermore, visual observation relies on crystal morphology to identify chemical composition, introducing the possibility of misclassification. This is particularly a concern in the early stages of scaling when crystals have yet to assume their distinct forms or in feed waters treated with antiscalants which can modify crystal morphologies. Consequently, the unique ability of the Raman sensor to provide chemical identification represents a critical advantage of the methodology (Table 6).

It should be noted that a direct comparison between Series I and II Raman detection times should be avoided due to the difference in each series' initial permeate fluxes, which in turn influence the degree of concentration polarization at the membrane surface (i.e., scaling propensity). Gypsum was detected after 95 ± 34 min of scaling and calcium carbonate was detected at 65 ± 32 min, corresponding to a mean flux decline of 8 ± 5 % and 4 ± 3 %, respectively. These flux decline values
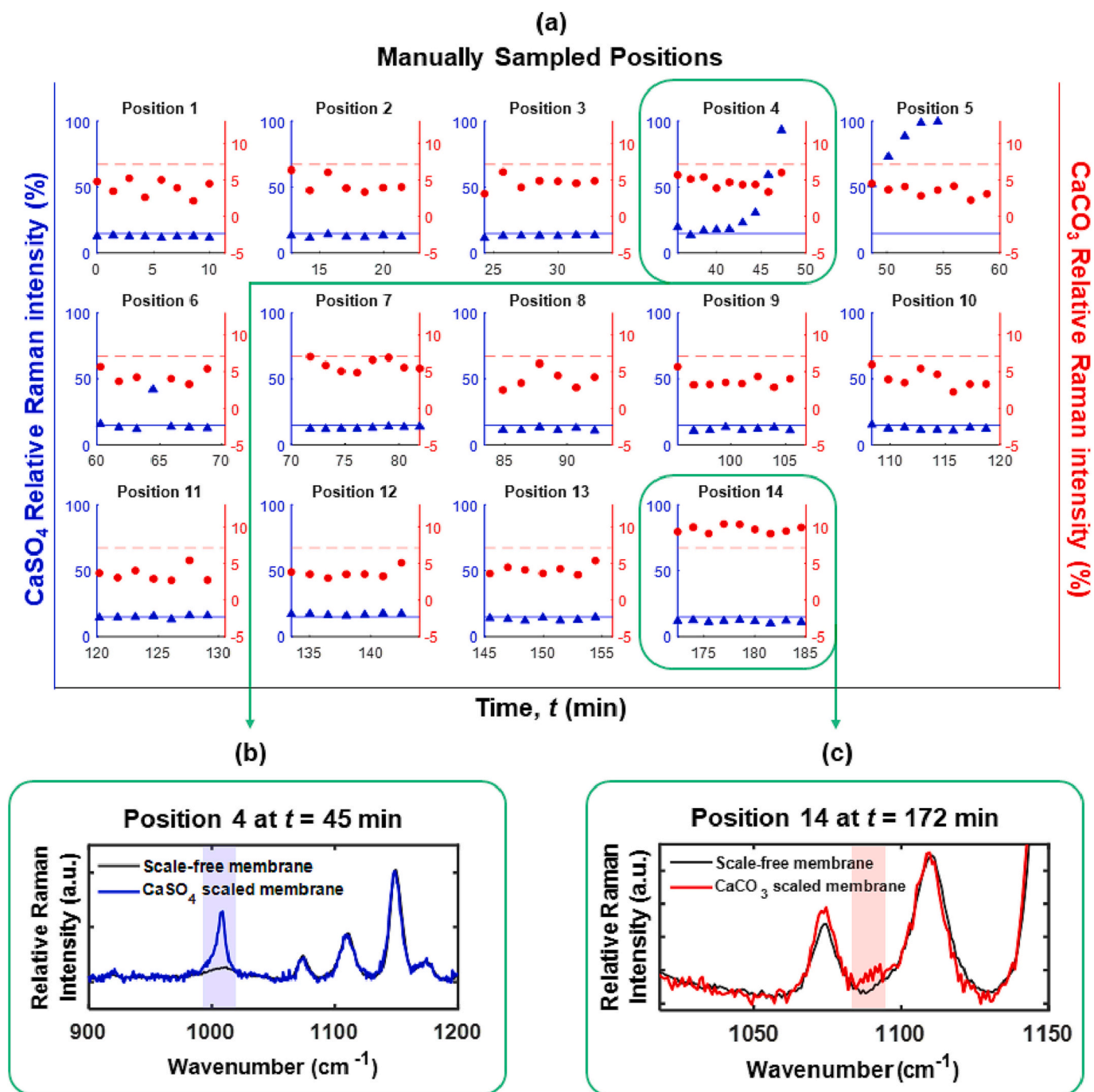
Fig. 5. (a) Series I representative real-time Raman data (Test 1) as a function of randomly selected position at (x_m, y_m), and time (t). Gypsum (blue triangle) was detected at the fourth randomly selected position (m = 4) at t = 45 min of salt feed filtration. Calcium carbonate (red circle) was detected at the 14th randomly selected position (m = 14) at t = 172 min of filtration. (b) The Raman spectrum from $t = 45$ min shows the ν_1 vibrational mode of gypsum at 1008 cm^{-1}. (c) The Raman spectrum from $t = 172$ min shows a broad band from 1086 to 1090 cm^{-1}, which is indicative of both the calcite and vaterite polymorphs of calcium carbonate. (For interpretation of the references to colour in this figure legend, the reader is referred to the web version of this article.)

are significantly lower values than those obtained from the manual sampling strategy for the Series I tests (13 ± 10 % and 22 ± 3 %, for calcium sulfate and calcium carbonate respectively). The lower values of flux decline (<10–15 % permeate flux decline) at the times of Series II Raman detection suggest that the modified sampling strategy improved early detection capability of both calcium carbonate and gypsum. However, further investigation on the selection of optimal sampling parameters is necessary to obtain meaningful scaling kinetics results, e. g., determining which scale formed first on the membrane surface as well as subsequent formation rates.

3.3. Post-mortem SEM imaging

Fig. 7 presents representative SEM images from Series I (manual sampling) and Series II (automated sampling) post-mortem membrane coupons. The presence of gypsum and calcium carbonate scaling crystals was visually confirmed for each test series. The micrographs clearly show that the average lateral dimensions of the calcium carbonate crystals are at least one order of magnitude smaller than those of gypsum crystals. The greater success of the Series II sampling strategy in detecting the smaller calcium carbonate crystals provides evidence that

Table 2
Summary of Series I Raman detection times for CaSO$_4$ membrane scaling as compared to the permeate flux decline at the time of Raman detection and the percentage of sampled points that resulted in a positive Raman detection result.

Test #	Raman Detection Time (min)	Permeate Flux Decline[a] (%)	Total Sampled Points (#)	Sampled Points with Positive Raman Detection (#)	Sampled Points with Positive Raman Detection (%)
1	39	1	14	3	21
2	127	20	12	2	17
3	133	18	19	8	42

[a] At the time of Raman detection.

Table 3
Summary of Series I Raman detection times for CaCO$_3$ membrane scaling as compared to the permeate flux decline at the time of Raman detection and the percentage of sampled points that resulted in a positive Raman detection result.

Test #	Raman detection time (min)	Permeate flux decline[a] (%)	Total sampled points (#)	Sampled points with positive Raman detection (#)	Sampled points with positive Raman detection (%)
1	170	19	14	1	7
2	141	24	12	1	8
3	174	24	19	2	11

[a] At the time of Raman detection.

an optimized sampling resolution can increase the probability of detecting smaller crystals such as calcium carbonate.

Calcium carbonate can form three main polymorphs, which are crystals that have the same chemical composition but a differing arrangement of lattice ions. The arrangement of the lattice ions results in different crystal morphologies and solubilities [60]. The upstream and downstream Series I calcium carbonate scaling crystals were predominantly spherical vaterite [61]. This supports the appearance of the 1090 cm^{-1} Raman band in Tests 1–3, belonging to the vaterite polymorph. Upstream and downstream Series II calcium carbonate crystals appear to exhibit a wider variety of shapes and sizes, including spherical vaterite, oval-shaped calcite [61], and "peanut-like" calcite and aragonite [62] (also reported as "broccoli" aragonite [63]). This visual observation also supports the real-time Raman data for Tests 4–9, which showed a broader Raman band encompassing the wavenumbers 1085 and 1086 cm^{-1}, belonging to the aragonite and calcite polymorph, respectively.

Calcium sulfate crystals belong to the monoclinic crystal system and feature a rosette-like growth pattern. Gypsum (CaSO$_4$·2H$_2$O) is the dominant calcium sulfate polymorph [2,8,17,19,54]. The fact that gypsum crystals presented themselves as rosettes serves as evidence that surface crystallization was the main scaling mechanism [1], as gypsum membrane scaling by bulk crystallization and subsequent deposition lacks this rosette-like form and instead appears to be a loose cake layer of gypsum rods or needles [18].

Despite the variability in scaling patterns between replicate test coupons [64], in general, we can observe greater surface coverage by gypsum scale (Fig. 7c) as compared to calcium carbonate scale. Indeed, a one order-of-magnitude difference in crystal size between the gypsum (~100 μm) and calcium carbonate (~10 μm) crystals can be observed. Given the laser beam spot size (~3 μm, full width at maximum height), there is a higher probability that gypsum will be fully situated under the fixed-coordinate laser beam. This was also noted in our previous work [53], where a single-point sampling scheme with a similar spot size was employed; in that work, only calcium sulfate was detected in real-time since the sampling scheme was not appropriately representative.

Indeed, the degree to which the sampled area is representative of the membrane scaling condition is a crucial element in the present development of the Raman-based, in situ monitoring technique. This work expanded the previous use of single-point sampling by employing a multi-point sampling strategy to increase the sampling area. This approach enabled the successful chemical detection of both calcium sulfate and calcium carbonate in real-time. Nonetheless, additional work is needed to investigate the spatial distribution of different scaling crystals, which is key to the selection of optimal sampling parameters.

Interestingly, in the Series I downstream SEM image (Fig. 7c), a trailing tail of platelets can be observed, nestled between the typically present gypsum rosettes. These particular platelets could be swallow-tail twins or Monmatre twins [65], which result from gypsum nucleation on a preexisting calcite surface and subsequent epitaxial growth [66]. In the formation of gypsum twins, dissolution of calcite crystals (host crystal) can provide calcium ions for the growth of the gypsum (guest crystal). Such an occurrence would suggest that calcium carbonate deposited first on the membrane surface. However, the post-mortem SEM images are only capable of providing a single snapshot in time of scaling progression. This further underscores the importance of being able to study the *spatiotemporal* interaction effects among multiple salt species, in real time. Such real-time chemical information afforded by Raman spectroscopy could play an important role in unraveling the complex kinetics of mixed-salt scaling.

3.4. Post-mortem gravimetric analysis

In bench-scale RO flow cells, the greater concentration polarization (CP) effects at downstream membrane surfaces, in contrast to upstream surfaces, serve as a greater source of scaling ions for scale formation [67]. Thus, membrane scaling is typically most severe near the channel exit (downstream). This expectation is supported by the gravimetric measurements shown in Fig. 8.

The downstream mean mass per area was 16 ± 2 % and 14 ± 9 % greater than the upstream values for Series I coupons (Tests 1–3) and Series II coupons (Tests 4–9), respectively. These results suggest that the scale progression from downstream to upstream locations was similar to that of single-component scaling [18,42], with greater downstream deposited mass. The measured scaling crystal mass per area (g/mm^2) increased with increasing normalized axial position, x/L, where x represents the axial position at the membrane from the feed inlet along the flow direction and L is the total length of the membrane. The mass per area of coupons from Test 6 did not show marked changes with increasing axial position. This result is unexpected and could reflect mass loss due to handling.

Overall, the ability of the current Raman sensor methodology for real-time concurrent detection of two scalants that considerably differ in size and distribution represents a significant step in the development of the methodology. Indeed, the methodology shows promise for the detection of additional major scalants on RO and NF membranes such as calcium phosphate [68,69]. Since scale-control techniques are highly sensitive to the chemical composition of the deposited scales [4], real-time chemical sensing is a crucial aspect of effective in-situ monitoring. Ongoing work using more sophisticated sensor configurations as well as optimized sampling techniques should enable improvements in detection accuracy and sensitivity that will facilitate application of the Raman sensor as the key component of a useful real-time detection methodology.

4. Conclusions

Chemical sensing is a critical capability for real-time monitoring techniques, especially for improved understanding of mixed-salt scaling dynamics during RO desalination. Furthermore, the success of many of the strategies used in scale control would benefit from accurate, real-time chemical identification of the scales. The present work reports
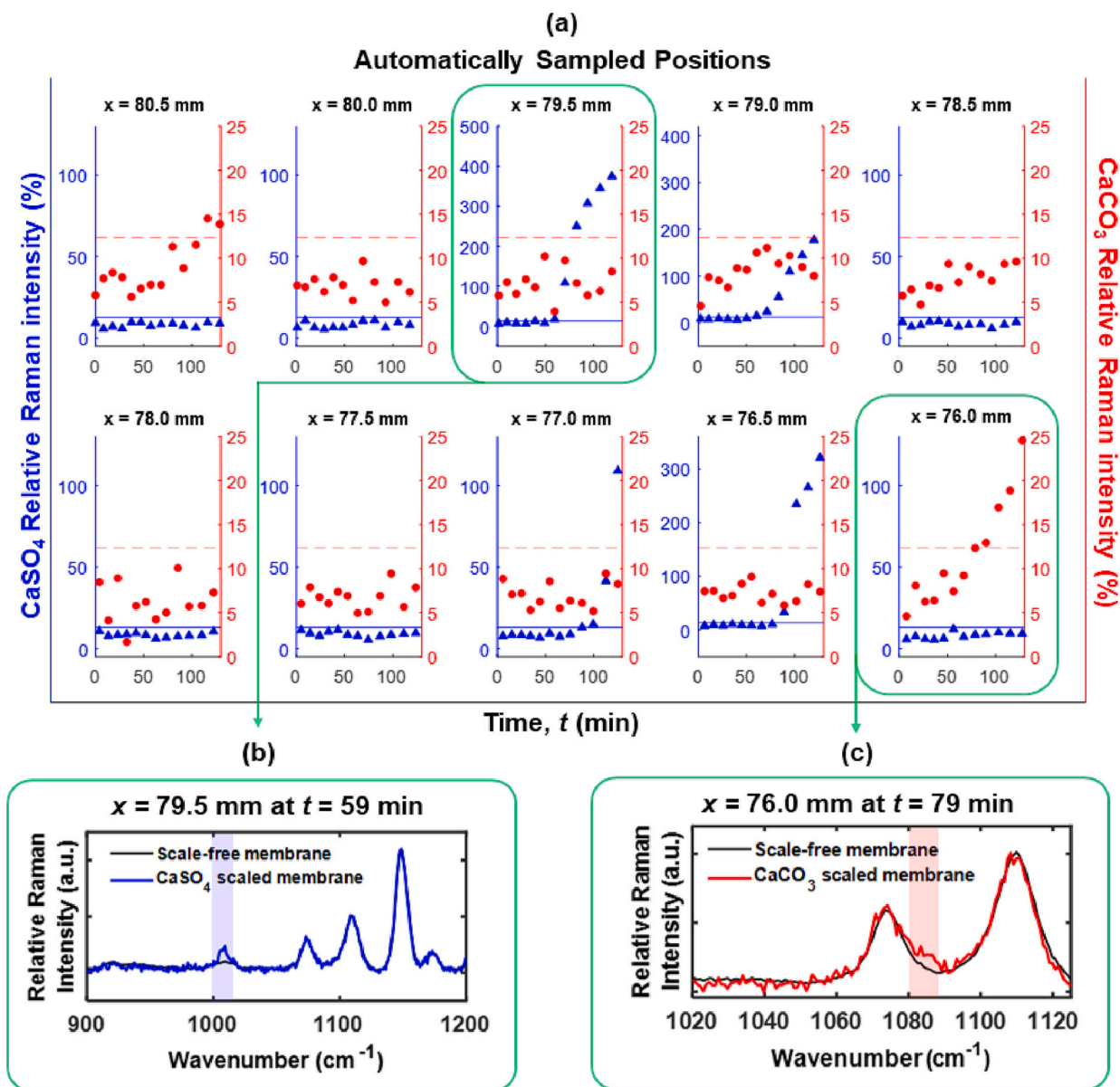
Fig. 6. (a) Series II representative real-time Raman data (Test 4) as a function of position (x) and time (t). Gypsum was first detected at $x = 79.5$ mm, at $t = 59$ min of salt feed filtration. Calcium carbonate was first detected at $x = 76.0$ mm, at $t = 79$ min. (b) The Raman spectrum from $t = 59$ min shows the v_1 vibrational mode of gypsum at 1008 cm^{-1}. (c) The Raman spectrum from $t = 79$ min shows a broad band from 1080 to 1086 cm^{-1}, which suggests the presence of amorphous calcium carbonate (ACC).

Table 4
Summary of Series II Raman detection times for CaSO$_4$ membrane scaling as compared to the permeate flux decline at the time of Raman detection, and the percentage of sampled points that resulted in a positive Raman detection result.

Test #	Raman Detection Time (min)	Permeate Flux Decline[a] (%)	Total Sampled Points (#)	Sampled Points with Positive Raman Detection (#)	Sampled Points with Positive Raman Detection (%)
4	59	2.1	10	4	40
5	124	10.8	10	1	10
6	–	–	10	0	0
7	133	13.8	10	1	10
8	94	9.6	10	3	30
9	63	4.2	10	3	30

[a] At the time of Raman detection.

Table 5
Summary of Series II Raman detection times for CaCO$_3$ membrane scaling as compared to the permeate flux decline at the time of Raman detection, and the percentage of sampled points that resulted in a positive Raman detection result.

Test #	Raman detection time (min)	Permeate flux decline[a] (%)	Total sampled points (#)	Sampled points with positive Raman detection (#)	Sampled points with positive Raman detection (%)
4	79	5.0	10	2	20
5	20	0.5	10	2	20
6	38	1.4	10	3	30
7	92	8.1	10	2	20
8	56	3.8	10	3	30
9	103	2.3	10	4	40

[a] At the time of Raman detection.

Table 6
Summary of advantages and disadvantages of real-time monitoring techniques.

Technique	References	Advantages	Disadvantages
Visual observation (e.g., EXSOD, MeMo)	[15–19]	Visual imaging techniques feature relatively large sampling areas. Images of the membrane surface provide information regarding localized scaling crystal growth kinetics and macroscopic development of crystal coverage on membranes over time.	Successful scale detection requires that crystals/crystal groups grow to ~50 μm in diameter or greater.
Ultrasonic Time-Domain Reflectometry (UTDR)	[20–23]	Noninvasive ultrasonic measurements can distinguish between membrane compaction and fouling layer growth, unlike flux-decline measurements. This method can be incorporated directly into spiral wound membranes (SWM), eliminating the need for a 'canary' cell.	Fouling studies that utilize UTDR are limited to detection of fouling layer growth but provide no information on fouling layer composition. UTDR detection of organic fouling is quite limited.
Electrical Impedance Spectroscopy (EIS)	[24–26]	EIS has been used to measure the thickness of electrically distinct layers in a membrane system and to investigate different fouling mechanisms (e.g., gel-layer formation, loose-cake formation). This method can also be incorporated directly into SWM.	EIS analyses yield area-averaged thickness measurements, which can present challenges in detecting spatially dependent changes on the membrane, such as scaling.
Raman spectroscopy	[29–32]	Raman spectroscopy provides chemical composition of fouling components with high spatial resolution.	The high spatial resolution of the technique can increase the likelihood of false negative detection results. This can be remedied by increasing the sampling area.
Optical Coherence Tomography (OCT)	[56–59]	OCT provides real-time thickness measurements of the fouling layer and is commonly used to study cake-layer growth. This technique has also been applied to successfully detect co-precipitating scalants based on crystal morphology.	The morphology of foulants may not be a reliable identifier of chemical composition, especially during the use of cleaning agents or antiscalants.

proof-of-concept demonstration of real-time, concurrent detection using Raman spectroscopy of two scaling salts during brackish water RO desalination. The static (fixed-coordinate) objective of a Raman microscope was integrated with a bench-scale RO crossflow cell mounted on a movable stage to enable multi-point Raman sampling during desalination. Replicate scaling experiments were conducted and real-time Raman data and permeate flux were recorded as a standard metric of comparison. Although local monitoring techniques may provide higher sensitivity to early onset scaling compared to global metrics, more localized measurements also run the risk of providing false negative detection results due to unrepresentative sampling. Thus, the performance of two different Raman sampling strategies was evaluated since representative, accurate scaling detection is a crucial aspect in the development of in-situ monitoring techniques.

In the first tested sampling strategy, a randomly selected, multi-point sampling scheme was employed to demonstrate the real-time Raman detection of both calcium carbonate and calcium sulfate scales. However, detection occurred inconsistently, with flux decline values of up to 24 % at the time of detection. To increase the consistency of Raman detection, a more systematic approach was utilized in a second sampling strategy featuring automated, multi-point sampling over a specified sampling length with a fixed sampling resolution. Here, flux declines as low as 2.1 % and 0.5 % were observed at the time of gypsum and calcium carbonate Raman detection, respectively. These results support the early detection capability and potential utility of the Raman sensor as a real-time decision-making tool during desalination plant operation. Results
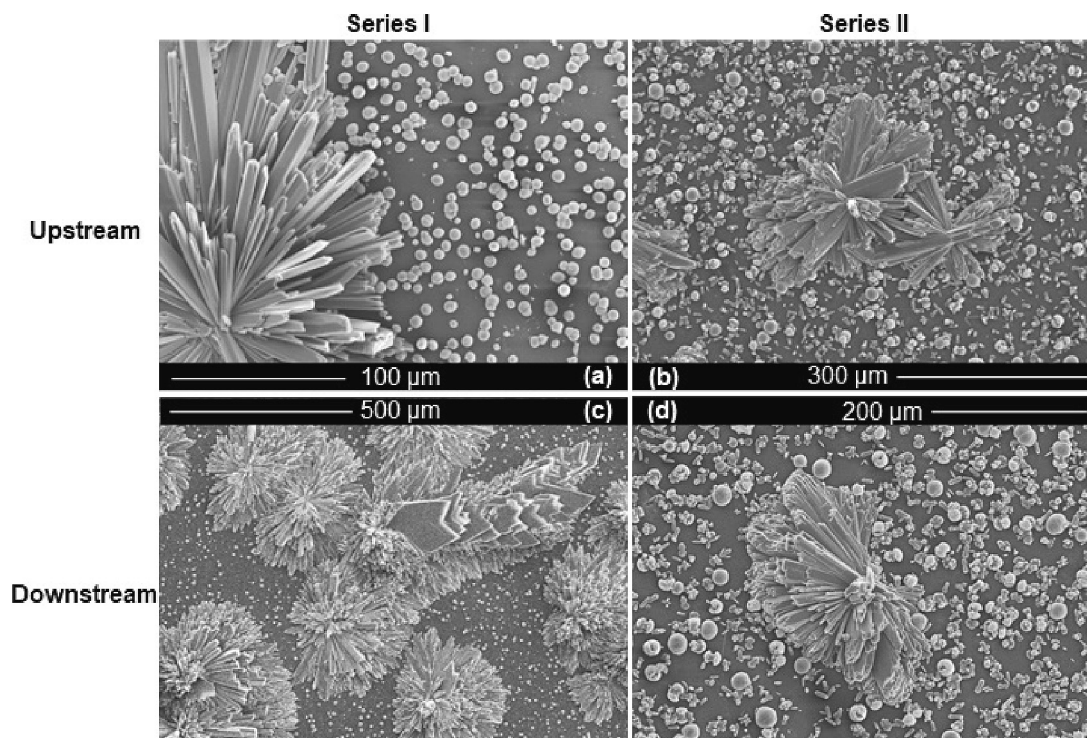
Fig. 7. Representative SEM images of calcium sulfate and calcium carbonate crystals from post-mortem membrane coupons: (a) Series I upstream, (b) Series II upstream, (c) Series I downstream, and (d) Series II downstream.
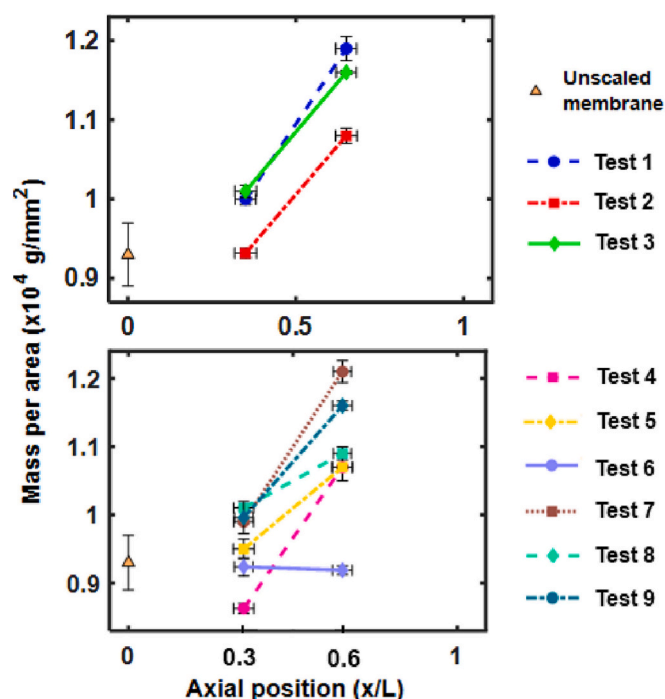
Fig. 8. Post-mortem gravimetric analysis from downstream and upstream membrane coupons from Tests 1–9. Upstream gravimetric measurements were taken at $x/L = 0.3$ and downstream values at $x/L = 0.6$.

also suggest that the Series II sampling strategy was better at detecting calcium carbonate (i.e., smaller scaling crystals), given the greater percentage of sampled points with a positive calcium carbonate detection result (27 ± 8 % in Series II vs 9 ± 2 % in Series I). Additional systematic experiments are necessary to validate these trends.

Post-mortem scanning electron microscopy of scaled membrane coupons confirmed the presence of both types of scaling crystals by visual inspection, where the calcium sulfate polymorph primarily featured a rosette structure consisting of rods and plates and calcium carbonate presented a more varied morphology depending on the polymorph. Gravimetric results indicated that the mass of deposited scales for two-component scaling followed a similar behavior as that of single-component scaling, with greater mass per area on downstream coupons compared to their upstream counterparts.

The current Raman sensor methodology was employed for a proof-of-concept demonstration of real-time, concurrent detection of multiple scalants. The two model scalants selected for study exhibited considerable differences in size and spatial distribution. Despite these differences in scalant characteristics, successful Raman detection was achieved. Consequently, the results of these initial experiments represent a significant step in the development of the methodology. We note that further research is required to explore the simultaneous Raman detection of inorganic and organic foulants. Organic foulants can be more challenging to study using Raman spectroscopy because they lack the long-range order of crystalline materials (inorganic foulants) [70], resulting in Raman signal broadening and reduced signal-to-noise ratios. Additionally, fluorescence cross-sections of organic foulants can be as much as 10^{14} times greater than their Raman cross-sections [71]. In other words, Raman signals from organic materials can be easily obscured by a large background signal comprised of fluorescence, noise, and membrane Raman signals, since polymeric membranes are also organic materials that could produce overlapping Raman bands. With continued improvement in instrumentation and sampling strategy, such as implementation of laser scanning microscopy, the methodology holds promise for effective early detection of membrane scaling during filtration of complex, more natural feed waters, enabling the implementation of more targeted and effective antifouling measures.

References

[1] S. Lee, Effect of operating conditions on CaSO4 scale formation mechanism in Nanofiltration for water softening, Water Res. 34 (15) (2000) 3854–3866.
[2] W.-Y. Shih, A. Rahardianto, R.-W. Lee, Y. Cohen, Morphometric characterization of calcium sulfate Dihydrate (gypsum) scale on reverse osmosis membranes, J. Membr. Sci. 252 (1–2) (2005) 253–263.
[3] S. Lee, C.H. Lee, Scale formation in NF/RO: mechanism and control, Water Sci. Technol. 51 (6–7) (2005) 9.
[4] A. Antony, J.H. Low, S. Gray, A.E. Childress, P. Le-Clech, G. Leslie, Scale formation and control in high pressure membrane water treatment systems: a review, J. Membr. Sci. 383 (1–2) (2011) 1–16.
[5] A. Matin, F. Rahman, H.Z. Shafi, S.M. Zubair, Scaling of reverse osmosis membranes used in water desalination: phenomena, impact, and control; future directions, Desalination 455 (2019) 135–157.
[6] M. Shmulevsky, X. Li, H. Shemer, D. Hasson, R. Semiat, Analysis of the onset of calcium sulfate scaling on RO membranes, J. Membr. Sci. 524 (2017) 299–304.
[7] A. Alshami, T. Taylor, N. Ismail, C. Buelke, L. Schultz, RO system scaling with focus on the concentrate line: current challenges and potential solutions, Desalination 520 (2021), 115370.
[8] M. Brusilovsky, J. Borden, D. Hasson, Flux decline due to gypsum precipitation on RO membranes, Desalination 86 (2) (1992) 187–222.
[9] J.S. Vrouwenvelder, J.A.M. van Paassen, J.C. Kruithof, M.C.M. van Loosdrecht, Sensitive pressure drop measurements of individual Lead membrane elements for accurate early biofouling detection, J. Membr. Sci. 338 (1–2) (2009) 92–99.
[10] M. Shmulevsky, X. Li, H. Shemer, D. Hasson, R. Semiat, Analysis of the onset of calcium sulfate scaling on RO membranes, J. Membr. Sci. 524 (2017) 299–304.
[11] T. Tran, B. Bolto, S. Gray, M. Hoang, E. Ostarcevic, An autopsy study of a fouled reverse osmosis membrane element used in a brackish water treatment plant, Water Res. 41 (17) (2007) 3915–3923.
[12] M. Raffin, E. Germain, S. Judd, Assessment of fouling of an RO process dedicated to indirect potable reuse, Desalin. Water Treat. 40 (1–3) (2012) 302–308.
[13] J. Kim, Autopsy of high-pressure membranes to compare effectiveness of MF and UF pretreatment in water reclamation, Water Res. 42 (3) (2007) 697–706.

[14] L.N. Sim, T.H. Chong, A.H. Taheri, S.T.V. Sim, L. Lai, W.B. Krantz, A.G. Fane, A review of fouling indices and monitoring techniques for reverse osmosis, Desalination 434 (2018) 169–188.

[15] A. Rahardianto, W.-Y. Shih, R.-W. Lee, Y. Cohen, Diagnostic characterization of gypsum scale formation and control in RO membrane desalination of brackish water, J. Membr. Sci. 279 (1–2) (2006) 655–668.

[16] M. Uchymiak, A. Rahardianto, E. Lyster, J. Glater, Y. Cohen, A novel RO ex situ scale observation detector (EXSOD) for mineral scale characterization and early detection, J. Membr. Sci. 291 (1–2) (2007) 86–95.

[17] A.R. Bartman, E. Lyster, R. Rallo, P.D. Christofides, Y. Cohen, Mineral scale monitoring for reverse osmosis desalination via real-time membrane surface image analysis, Desalination 273 (1) (2011) 64–71.

[18] J. Benecke, J. Rozova, M. Ernst, Anti-scale effects of select organic macromolecules on gypsum bulk and surface crystallization during reverse osmosis desalination, Sep. Purif. Technol. 198 (2018) 68–78.

[19] N.R. Sarker, A.M. Bilton, Real-time computational imaging of reverse osmosis membrane scaling under intermittent operation, J. Membr. Sci. 636 (2021), 119556.

[20] A.P. Mairal, A.R. Greenberg, W.B. Krantz, L.J. Bond, Real-time measurement of inorganic fouling of RO desalination membranes using ultrasonic time-domain reflectometry, J. Membr. Sci. 159 (1) (1999) 185–196.

[21] J. Li, Direct monitoring of membrane fouling and cleaning during ultrafiltration using a non-invasive ultrasonic technique, J. Membr. Sci. 215 (1–2) (2003) 33–52.

[22] G. An, J. Lin, J. Li, X. Li, X. Jian, Non-invasive measurement of membrane scaling and cleaning in spiral-wound reverse osmosis modules by ultrasonic time-domain reflectometry with sound intensity calculation, Desalination 283 (2011) 3–9.

[23] X. Lu, E. Kujundzic, G. Mizrahi, J. Wang, K. Cobry, M. Peterson, J. Gilron, A. R. Greenberg, Ultrasonic sensor control of flow reversal in RO desalination—part 1: mitigation of calcium sulfate scaling, J. Membr. Sci. 419–420 (2012) 20–32.

[24] A. Antony, T. Chilcott, H. Coster, G. Leslie, In situ structural and functional characterization of reverse osmosis membranes using electrical impedance spectroscopy, J. Membr. Sci. 425–426 (2013) 89–97.

[25] Z. Hu, A. Antony, G. Leslie, P. Le-Clech, Real-time monitoring of scale formation in reverse osmosis using electrical impedance spectroscopy, J. Membr. Sci. 453 (2014) 320–327.

[26] J. Cen, M. Vukas, G. Barton, J. Kavanagh, H.G.L. Coster, Real time fouling monitoring with electrical impedance spectroscopy, J. Membr. Sci. 484 (2015) 133–139.

[27] S.A. Creber, J.S. Vrouwenvelder, M.C.M. van Loosdrecht, M.L. Johns, Chemical cleaning of biofouling in reverse osmosis membranes evaluated using magnetic resonance imaging, J. Membr. Sci. 362 (1) (2010) 202–210.

[28] N.W. Bristow, S.J. Vogt, S.S. Bucs, J.S. Vrouwenvelder, M.L. Johns, E. O. Fridjonsson, Novel magnetic resonance measurements of fouling in operating spiral wound reverse osmosis membrane modules, Water Res. 196 (2021), 117006.

[29] T. Virtanen, S.-P. Reinikainen, M. Kögler, M. Mänttäri, T. Viitala, M. Kallioinen, Real-time fouling monitoring with Raman spectroscopy, J. Membr. Sci. 525 (2017) 312–319.

[30] M. Kögler, B. Zhang, L. Cui, Y. Shi, M. Yliperttula, T. Laaksonen, T. Viitala, K. Zhang, Real-time Raman based approach for identification of biofouling, Sensors Actuators B Chem. 230 (2016) 411–421.

[31] O.D. Supekar, J.J. Brown, A.R. Greenberg, J.T. Gopinath, V.M. Bright, Real-time detection of reverse-osmosis membrane scaling via Raman spectroscopy, Ind. Eng. Chem. Res. (2018) 16021–16026.

[32] O.D. Supekar, D.J. Park, A.R. Greenberg, J.T. Gopinath, V.M. Bright, Real-time detection of early-stage calcium sulfate and calcium carbonate scaling using Raman spectroscopy, J. Membr. Sci. 596 (2019) 117603.

[33] T.H. Chong, R. Sheikholeslami, Thermodynamics and kinetics for mixed calcium carbonate and calcium sulfate precipitation, Chem. Eng. Sci. 56 (18) (2001) 5391–5400.

[34] M. Sudmalis, R. Sheikholeslami, Coprecipitation of CaCO3 and CaSO4, Can. J. Chem. Eng. 78 (1) (2000) 21–31.

[35] Y. Yan, T. Yu, H. Zhang, J. Song, C. Qu, J. Li, B. Yang, Co-deposition mechanisms of calcium sulfate and calcium carbonate scale in produced water, Crystals 11 (12) (2021) 1494.

[36] I. Koyuncu, M.R. Wiesner, Morphological variations of precipitated salts on NF and RO membranes, Environ. Eng. Sci. 24 (5) (2007) 602–614.

[37] P. Brüesch, Phonons: Theory and Experiments I, Springer Berlin Heidelberg, Berlin, Heidelberg, 1982.

[38] Le Ru, E., and Etchegoin, P., Principles of surface-enhanced Raman spectroscopy: and related plasmonic effects, Elsevier Science and Technology Books, Inc.

[39] A. Spinthaki, K.D. Demadis, Chemical methods for scaling control, in: V.S. Saji, A. A. Meroufel, A.A. Sorour (Eds.), Corrosion and Fouling Control in Desalination Industry, Springer International Publishing, Cham, 2020, pp. 307–342.

[40] J. Rolf, T. Cao, X. Huang, C. Boo, Q. Li, M. Elimelech, Inorganic scaling in membrane desalination: models, mechanisms, and characterization methods, Environ. Sci. Technol. 56 (12) (2022) 7484–7511.

[41] T. Virtanen, P. Parkkila, A. Koivuniemi, J. Lahti, T. Viitala, M. Kallioinen, M. Mänttäri, A. Bunker, Characterization of membrane–foulant interactions with novel combination of raman spectroscopy, surface plasmon resonance and molecular dynamics simulation, Sep. Purif. Technol. 205 (2018) 263–272.

[42] D.J. Park, O.D. Supekar, A.R. Greenberg, J.T. Gopinath, V.M. Bright, Real-time monitoring of calcium sulfate scale removal from RO desalination membranes using Raman spectroscopy, Desalination 497 (2021), 114736.

[43] A. Rahardianto, B.C. McCool, Y. Cohen, Reverse osmosis desalting of inland brackish water of high gypsum scaling propensity: kinetics and mitigation of membrane mineral scaling, Environ. Sci. Technol. 42 (12) (2008) 4292–4297.

[44] D.J. Park, O.D. Supekar, A.R. Greenberg, J.T. Gopinath, V.M. Bright, In-situ monitoring of calcium carbonate scale progression on reverse osmosis membranes using Raman spectroscopy, DWT 273 (2022) 92–103.

[45] N. Prieto-Taboada, O. Gómez-Laserna, I. Martínez-Arkarazo, M.Á. Olazabal, J. M. Madariaga, Raman spectra of the different phases in the CaSO4–H2O system, Anal. Chem. 86 (20) (2014) 10131–10137.

[46] C. Carteret, A. Dandeu, S. Moussaoui, H. Muhr, B. Humbert, E. Plasari, Polymorphism studied by lattice phonon Raman spectroscopy and statistical mixture analysis method. Application to calcium carbonate polymorphs during batch crystallization, Cryst. Growth Des. 9 (2) (2009) 807–812.

[47] H.J. Kim, A.E. Fouda, K. Jonasson, In situ study on kinetic behavior during asymmetric membrane formation via phase inversion process using Raman spectroscopy, J. Appl. Polym. Sci. 75 (1) (2000) 135–141.

[48] K.D. Cobry, Z. Yuan, J. Gilron, V.M. Bright, W.B. Krantz, A.R. Greenberg, Comprehensive experimental studies of early-stage membrane scaling during Nanofiltration, Desalination 283 (2011) 40–51.

[49] D.L. Parkhurst, User's Guide to PHREEQC, a Computer Program for Speciation, Reaction-Path, Advective-Transport, and Inverse Geochemical Calculations, 95–4227, U.S. Geological Survey, Reston, VA, 1995.

[50] R. Singh, Water and Membrane Treatment, Elsevier, Membrane Technology and Engineering for Water Purification, 2015, pp. 81–178.

[51] U. Wehrmeister, D.E. Jacob, A.L. Soldati, N. Loges, T. Häger, W. Hofmeister, Amorphous, Nanocrystalline and crystalline calcium carbonates in biological materials, J. Raman Spectrosc. 42 (5) (2011) 926–935.

[52] S. Mitrouli, A.J. Karabelas, A. Karanasiou, M. Kostoglou, Incipient calcium carbonate scaling of desalination membranes in narrow channels with spacers—experimental insights, J. Membr. Sci. 425–426 (2013) 48–57.

[53] O.D. Supekar, D.J. Park, A.R. Greenberg, J.T. Gopinath, V.M. Bright, Real-time detection of early-stage calcium sulfate and calcium carbonate scaling using Raman spectroscopy, J. Membr. Sci. 596 (2020), 117603.

[54] T. Waly, M.D. Kennedy, G.-J. Witkamp, G. Amy, J.C. Schippers, The role of inorganic ions in the calcium carbonate scaling of seawater reverse osmosis systems, Desalination 284 (2012) 279–287.

[55] A.J. Karabelas, A. Karanasiou, S.T. Mitrouli, Incipient membrane scaling by calcium sulfate during desalination in narrow spacer-filled channels, Desalination 345 (2014) 146–157.

[56] Y. Gao, S. Haavisto, W. Li, C.Y. Tang, J. Salmela, A.G. Fane, Novel approach to characterizing the growth of a fouling layer during membrane filtration via optical coherence tomography, Environ. Sci. Technol. 48 (24) (2014) 14273–14281.

[57] S. West, M. Wagner, C. Engelke, H. Horn, Optical coherence tomography for the in situ three-dimensional visualization and quantification of feed Spacer Channel fouling in reverse osmosis membrane modules, J. Membr. Sci. 498 (2016) 345–352.

[58] S. Lee, H. Cho, Y. Choi, S. Lee, Application of optical coherence tomography (OCT) to analyze membrane fouling under intermittent operation, Membranes 13 (4) (2023) 392.

[59] T.P. Pham Le, M.S. Jouini, A. Al Masri Alwan, S. Agashichev, M. AlSuwaidi, E. Alhseinat, Optical coherence tomography and digital image processing for scaling and co-precipitation investigation on reverse osmosis membrane, J. Membr. Sci. 677 (2023), 121658.

[60] R.A. Boulos, F. Zhang, E.S. Tjandra, A.D. Martin, D. Spagnoli, C.L. Raston, Spinning up the polymorphs of calcium carbonate, Sci. Rep. 4 (1) (2015) 3616.

[61] C.Y. Tai, F.-B. Chen, Polymorphism of CaCO3, precipitated in a constant-composition environment, AICHE J. 44 (8) (1998) 1790–1798.

[62] H. Tang, J. Yu, X. Zhao, Controlled synthesis of crystalline calcium carbonate aggregates with unusual morphologies involving the phase transformation from amorphous calcium carbonate, Mater. Res. Bull. 44 (4) (2009) 831–835.

[63] J.W. Morse, R.S. Arvidson, A. Lüttge, Calcium carbonate formation and dissolution, Chem. Rev. 107 (2) (2007) 342–381.

[64] J. Benecke, M. Haas, F. Baur, M. Ernst, Investigating the development and reproducibility of heterogeneous gypsum scaling on reverse osmosis membranes using real-time membrane surface imaging, Desalination 428 (2018) 161–171.

[65] L. Pastero, R. Giustetto, D. Aquilano, Calcite passivation by gypsum: the role of the cooperative effect, CrystEngComm 19 (26) (2017) 3649–3659.

[66] E. Ruiz-Agudo, P. Álvarez-Lloret, A. Ibañez-Velasco, M. Ortega-Huertas, Crystallographic control in the replacement of calcite by calcium sulfates, Cryst. Growth Des. 16 (9) (2016) 4950–4959.

[67] J.C. Chen, Q. Li, M. Elimelech, In situ monitoring techniques for concentration polarization and fouling phenomena in membrane filtration, Adv. Colloid Interf. Sci. 107 (2) (2004) 83–108.

[68] G. Greenberg, D. Hasson, R. Semiat, Limits of RO recovery imposed by calcium phosphate precipitation, Desalination 183 (1–3) (2005) 273–288.

[69] B. Han, M. Louhi-Kultanen, Real-time Raman monitoring of calcium phosphate precipitation in a semi-batch stirred crystallizer, Cryst. Growth Des. 18 (3) (2018) 1622–1628.

[70] R. Loudon, The Raman effect in crystals, Adv. Phys. 50 (7) (2001) 813–864.

[71] Z. Li, J. Wang, D. Li, Applications of Raman spectroscopy in detection of water quality, Appl. Spectrosc. Rev. 51 (4) (2016) 333–357.